Neutron Capture on the s-Process Branching Point 171Tm via Time-of-Flight and Activation

Rukelj, Z.; Homes, C. C.; Orlita, M.; Akrap, Ana

Journal article, Published version
Rad u časopisu, Objavljena verzija rada (izdavačev PDF)

Permanent link / Trajna poveznica: https://urn.nsk.hr/urn:nbn:hr:217:289032

Download date / Datum preuzimanja: **2025-03-26**

Repository / Repozitorij:

Repository of the Faculty of Science - University of Zagreb

Distinguishing the gapped and Weyl semimetal scenario in ZrTe$_5$: Insights from an effective two-band model

Z. Rukelj,[1,2,*] C. C. Homes,[3] M. Orlita,[4,5] and Ana Akrap [1,†]

[1]*Department of Physics, University of Fribourg, 1700 Fribourg, Switzerland*
[2]*Department of Physics, Faculty of Science, University of Zagreb, Bijenička c. 32, 10000 Zagreb, Croatia*
[3]*Condensed Matter Physics and Materials Science Division, Brookhaven National Laboratory, Upton, New York 11973, USA*
[4]*LNCMI, CNRS-UGA-UPS-INSA, 25, avenue des Martyrs, F-38042 Grenoble, France*
[5]*Institute of Physics, Charles University in Prague, CZ-12116 Prague, Czech Republic*

Here we study the static and dynamic transport properties of a low-energy two-band model proposed previously in Martino *et al.* [PRL **122**, 217402 (2019)], with an anisotropic in-plane linear momentum dependence and a parabolic out-of-plane dispersion. The model is extended to include a negative band gap, which leads to the emergence of a Weyl semimetal (WSM) state, as opposed to the gapped semimetal (GSM) state when the band gap is positive. We calculate and compare the zero- and finite-frequency transport properties of the GSM and WSM cases. The DC properties that are calculated for the GSM and WSM cases are Drude spectral weight, mobility, and resistivity. We determine their dependence on the Fermi energy and crystal direction. The in- and out-of-plane optical conductivities are calculated in the limit of the vanishing interband relaxation rate for both semimetals. The main common features are an $\omega^{1/2}$ in-plane and $\omega^{3/2}$ out-of-plane frequency dependence of the optical conductivity. We seek particular features related to the charge transport that could unambiguously point to one ground state over the other, based on the comparison with the experiment. Differences between the WSM and GSM are in principle possible only at extremely low carrier concentrations and at low temperatures.

I. INTRODUCTION

Zirconium pentatelluride, ZrTe$_5$, is a layered material [1–4] which recently became a topic of intense research. This was mainly due to the experimental evidence [5–7] of a 3D Dirac (3DD)-like band structure in the vicinity of the Γ point of the Brillouin zone, compared with the previously held belief of paraboliclike valence bands [3]. One of the major signatures of a 3DD-like band structure is the linearity in the optical conductivity with respect to photon energy $\hbar\omega$ above the Pauli threshold [8]. However, for ZrTe$_5$, recent optical and magneto-optical measurements [9] suggest that the energy bands are not entirely linear but posses an out-of-plane parabolic term as well.

As in many other topological semimetals, in ZrTe$_5$ the intrinsic energy scales are small. This makes it challenging to experimentally distinguish between different possible ground states [10]. The ambiguity of the band gap—whether it is zero, finite, and positive or finite and negative—also opens a possibility that ZrTe$_5$ may be a Weyl semimetal (WSM) [11] and not a Dirac semimetal as previously stated [12,13]. To distinguish between these two options, it is of interest to see how much their calculated charge transport quantities differ. This begs the question of whether one could interpret the same experimental data in different ways.

Based on the experiment and the *ab initio* calculation, we had previously introduced a simple low-energy two-band model for ZrTe$_5$, which was identified as a gapped semimetal. The main features of the proposed effective Hamiltonian are the gapped and electron-hole symmetric eigenvalues. This is accompanied by the anisotropic linearity of the bands along the intralayer (x, y) directions and the parabolic dispersion in the weakly dispersive out-of-plane z direction. This model provided an explanation of experimental data [9,14], in particular the square-root dependence of the optical conductivity at very low photon energies, in contrast to the linear dependence found in 3DD semimetals [8,15,16]. It also allowed us to estimate the energy interval in which the simple two-band model applies.

In this paper, we identify under which circumstances it is possible to distinguish between the gapped and WSM scenario, specifically for ZrTe$_5$. To do this, we generalize the Hamiltonian model to allow for a negative band gap [17–19]. By this simple change of the sign of the band gap, we generate a minimal 2×2 model Hamiltonian for WSM. And so, by changing the sign of this parameter, we pass from a gapped semimetal (GSM) to the WSM. The main difference lies in the shape of the bands at low energies. Contrary to the GSM case, the WSM case has a 3D linearlike bands in the close vicinity of the two Weyl points.

In the $\omega = 0$ case, corresponding to DC transport, we calculate the total and the effective concentration of electrons. Since the effective concentration is direction dependent, it will explain the resistivity anisotropy as well as the carrier mobility.
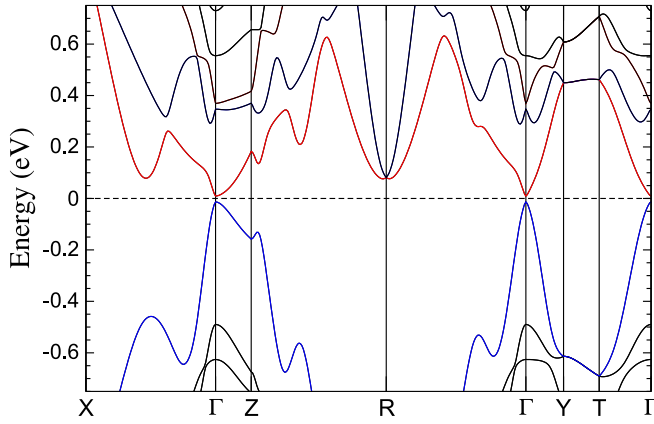
*zrukelj@phy.hr
†ana.akrap@unifr.ch

FIG. 1. *Ab initio* calculated band structure of ZrTe$_5$. The valence and the conduction bands are drawn in blue and red, respectively.

All three spatial components of the real part of the interband conductivity are evaluated for GSM and WSM cases, in the limit of vanishing relaxation rate. We find that for both the GSM and WSM, at high photon energies the (x, y) plane conductivity has a $(\hbar\omega)^{1/2}$ dependence, and in the z direction it has a $(\hbar\omega)^{3/2}$ dependence when the external field energies are well above the band-gap value. For photon energies below the band gap, the GSM optical conductivity is zero, while the WSM shows a $\hbar\omega$ dependence, similar to the 3DD case.

Finite temperatures, with $k_B T$ comparable to the Fermi energy, significantly alter the shape of the optical conductivity. This results in a linearlike optical conductivity, which can easily be mistaken for a signature of a gapless 3DD dispersion. Finite interband relaxation values only slightly modify the general appearance of the real part of the conductivity, except in the band-gap region where the conductivity acquires a finite contribution proportional to the relaxation itself.

II. *AB INITIO* CALCULATIONS AND THE MODEL HAMILTONIAN

We have performed *ab initio* band-structure calculations of the orthorhombic *Cmcm* phase of ZrTe$_5$ using density-functional theory (DFT) with the generalized gradient approximation [20–22]. Once the unit cell is finalized with the parameters $a = 4.06$ Å, $b = 14.76$ Å, and $c = 13.97$ Å, a spin-orbit coupling is added to the electronic-structure calculations. The results are shown in Fig. 1 with the valence band in blue and the conduction band in red.

At small energies, the material appears to be a semimetal with a small band gap and the quasilinear features in the vicinity of the Γ point in the Brillouin zone. The effective model considered in Ref. [9]—and used throughout the present paper—is based on these basic features of the calculated band structure. We estimate that this two-band model is valid in the energy interval of 60 meV above and below the band gap. Outside this interval, the experimental optical conductivity and the theoretical calculation no longer match. However, the problem lies in the values of the *ab initio* calculated parameters in Table I. These parameters are obtained by fitting the dispersions Eq. (2.2) to the DFT conduction band up to 60 meV in all three directions (x, y, z). As seen from

TABLE I. The values of the parameters entering Hamiltonian (2.1). The parameters Δ and ε_F are taken from the magneto-optical measurements [9] while velocities and effective mass have been calculated based on the comparison of the theoretical predictions of the GSM model and the experimental values.

	v_x(m/s)	v_y(m/s)	m^*/m_e	2Δ(meV)	ε_F(meV)
exp	7×10^5	5×10^5	2	6	14
DFT	3×10^5	2×10^5	1	20	0

Table I, the DFT parameters deviate from the experimentally determined parameters [9]. In particular, the band gap 2Δ is off by a factor of 3, and in some references a factor of 10 or more [23–25]. The band gap is difficult to establish yet it defines the ground state of ZrTe$_5$. In this paper, we also allow the possibility that ZrTe$_5$ is a WSM, suggested by some studies [11].

A. Effective two-band model

The 2×2 Hamiltonian matrix implements the electron-hole symmetry of the valence bands, a positive energy band gap 2Δ originating from the spin-orbit coupling, with the assumption of a free-electron-like behavior in the z (or b axis) direction and linear energy dependence in the x, y (a, c) plane. Here we expand the model to account for the Weyl phase by adding a negative band gap. The Hamiltonian is thus

$$\hat{H}_\nu = \hbar v_x k_x \sigma_x + \hbar v_y k_y \sigma_y + \left(\hbar^2 c^2 k_z^2 + \nu\Delta\right)\sigma_z, \quad (2.1)$$

where the label ν differentiates between the GSM for the value $\nu = +1$, and the WSM for the value $\nu = -1$. Further, $\sigma_{x,y,z}$ are Pauli matrices, $v_{x,y}$ are the velocities in the x and y directions, and we introduce $c^2 = 1/2m^*$ with m^* being the effective mass.

The diagonalization of Eq. (2.1) gives electron-hole symmetric eigenvalues

$$\varepsilon_\nu^{c,v}(\mathbf{k}) = \pm\sqrt{(\hbar v_x k_x)^2 + (\hbar v_y k_y)^2 + \left(\hbar^2 c^2 k_z^2 + \nu\Delta\right)^2}, \quad (2.2)$$

with the indices for the conduction (c) and valence (v) bands. Although trivial, the change from $\Delta \to -\Delta$ significantly alters the energies and single-particle properties. While the GSM phase is always gapped in this model, the WSM phase has two Weyl points in the Brillouin zone where the energy vanishes, $(k_x^w, k_y^w, k_z^w) = (0, 0, \pm\sqrt{\Delta}/\hbar c)$. Expanding the WSM eigenvalues around these two points gives linear momentum eigenvalues,

$$\varepsilon_W^{c,v}(\mathbf{k} - \mathbf{k}^w) = \pm\sqrt{(\hbar v_x k_x)^2 + (\hbar v_y k_y)^2 + (\hbar v_z k_z)^2}, \quad (2.3)$$

where we can formally identify

$$v_z^2 = 4\Delta c^2 = 2\Delta/m^*. \quad (2.4)$$

In a third, trivial phase, a zero gap phase occurs when the band gap is set to zero, $\Delta = 0$.

For $\Delta > 0$, we have a gapped phase in which the gap is k_z dependent but never changes its sign. Therefore, there is no interesting topology involved [26]. In contrast, for $\Delta < 0$, we obtain a minimal model for a WSM. This model is spin degenerate simply because the Hamiltonian matrix is 2×2 and

not 4×4. Spin degeneracy is ensured by the centrosymmetric lattice of ZrTe$_5$. Still, because we gain in simplicity, it is fitting to call this $\Delta < 0$ phase in a 2×2 Hamiltonian model a WSM phase [17,27,28].

B. Density of states

Here we calculate the density of states (DOS) for the energy dispersion from Eq. (2.2) for the GSM and WSM cases. By definition, the DOS per unit volume is

$$g(\varepsilon) = \frac{2}{V} \sum_{\mathbf{k}} \delta(\varepsilon - \varepsilon_{\mathbf{k}}). \qquad (2.5)$$

Given the shape of the dispersions in Eq. (2.2), the sum is changed into an integral in a cylindrical coordinate system by introducing the variables $\varrho^2 = (\hbar v_x k_x)^2 + (\hbar v_y k_y)^2$ and $z = \hbar c k_z$,

$$g_\nu(\varepsilon) = \frac{2}{(2\pi)^3} \frac{1}{\hbar^3} \frac{1}{v_x v_y c} \int \varrho \, d\varrho \int_0^{2\pi} d\varphi$$
$$\times \int dz \, \delta(\varepsilon - \sqrt{\varrho^2 + (z^2 + \nu\Delta)^2}). \qquad (2.6)$$

First, the delta function in Eq. (2.6) is decomposed with respect to the z variable into a sum:

$$\delta(\ldots) = \sum_{z_0} \delta(z - z_0) \left| \frac{\sqrt{\varrho^2 + (z_0^2 + \nu\Delta)^2}}{2z_0(z_0^2 + \nu\Delta)} \right|. \qquad (2.7)$$

Here, z_0 are the four roots of the argument within the δ function: $z_0 = \pm\sqrt{\pm\sqrt{\varepsilon^2 - \varrho^2} - \nu\Delta}$. Due to the absolute value, the outer set of $\pm$ points only brings a factor of 2 in Eq. (2.6). The $p = \pm 1$ under the square root is relevant for further evaluation, as it will determine the upper limit of the integration for ϱ. Inserting Eq. (2.7) in Eq. (2.6), and by noticing that $\varepsilon = \sqrt{\varrho^2 + (z_0^2 + \nu\Delta)^2}$, we have

$$g_\nu(\varepsilon) = \frac{1}{2\pi^2} \frac{1}{\hbar^3} \frac{\varepsilon}{v_x v_y c} \sum_p \int \frac{\varrho \, d\varrho}{\sqrt{\varepsilon^2 - \varrho^2}} \sqrt{p\sqrt{\varepsilon^2 - \varrho^2} - \nu\Delta}. \qquad (2.8)$$

The upper limit of the ϱ integration is determined by the condition that the expression under the square root in Eq. (2.8) be positive. The first obvious constraint is $\varrho < \varepsilon$, and the second depends on the sign p and on the type ν.

We solve the WSM case ($\nu = -1$) first. For $p = 1$, the subroot expression is well defined if $\varrho < \varepsilon$. For $p = -1$, we have two additional constraints. If $\varepsilon < \Delta$, then $0 < \varrho < \varepsilon$, or else if $\varepsilon > \Delta$, then $\sqrt{\varepsilon^2 - \Delta^2} < \varrho < \varepsilon$. The integral in Eq. (2.8) for the WSM case with the constraints on ϱ can be most simply written by introducing the variable $u = \sqrt{\varepsilon^2 - \Delta^2}$. Then

$$g_W(\varepsilon) = \frac{1}{2\pi^2} \frac{1}{\hbar^3} \frac{\varepsilon}{v_x v_y c} \times$$
$$\left(\int_0^\varepsilon \frac{du}{\sqrt{u + \Delta}} + \int_0^\varepsilon \frac{\Theta(\Delta - \varepsilon) \, du}{\sqrt{-u + \Delta}} + \int_0^\Delta \frac{\Theta(\varepsilon - \Delta) \, du}{\sqrt{-u + \Delta}} \right), \qquad (2.9)$$
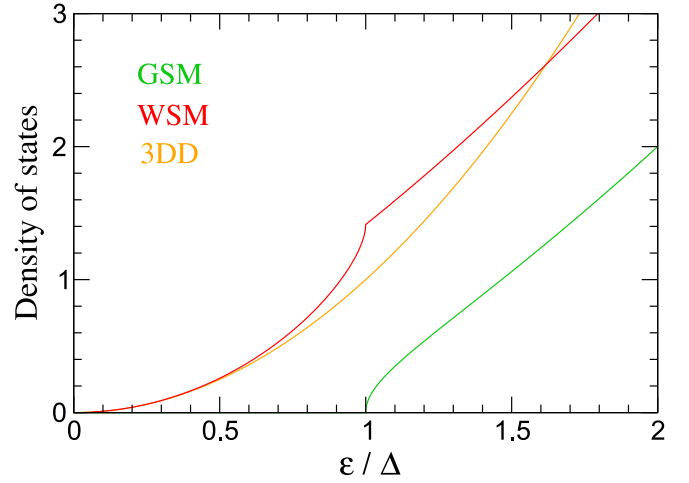
FIG. 2. The density of states (DOS) as a function of ε/Δ in units of $g_0 \Delta^{3/2}$ [defined in Eq. (2.11)] is shown for three cases: Weyl semimetal [Eq. (2.12)], gapped semimetal [Eq. (2.14)], and 3D Dirac dispersion [Eq. (2.15)]. At $\varepsilon \ll \Delta$, the DOS for the Weyl case and 3D Dirac dispersion coincide.

where Θ is the Heaviside step function. If we introduce an auxiliary function $\mathscr{G}(\varepsilon, \Delta)$,

$$\mathscr{G}(\varepsilon, \Delta) = \varepsilon\sqrt{\varepsilon - \Delta}, \qquad (2.10)$$

and the unit g_0 as

$$g_0 = \frac{1}{\pi^2 \hbar^3} \frac{1}{v_x v_y c}, \qquad (2.11)$$

we can write the final result for DOS:

$$g_W(\varepsilon) = g_0[\mathscr{G}(\varepsilon, -\Delta)\Theta(\varepsilon - \Delta)$$
$$+ (\mathscr{G}(\varepsilon, -\Delta) + \mathscr{G}(-\varepsilon, -\Delta))\Theta(\Delta - \varepsilon)]. \qquad (2.12)$$

The GSM case ($\nu = 1$) follows similarly. Inspecting the subroot function in Eq. (2.8), we see that $p = -1$ makes the subroot expression negative and so we discard it. On the other hand, $p = +1$ restricts ϱ to $0 < \varrho < \sqrt{\varepsilon^2 - \Delta^2}$. From the upper limit, we conclude that $\varepsilon > \Delta$. Using the same substitution as in the WSM case, we have

$$g_G(\varepsilon) = \frac{1}{2\pi^2} \frac{1}{\hbar^3} \frac{\varepsilon}{v_x v_y c} \int_\Delta^\varepsilon \frac{du}{\sqrt{u + \Delta}}, \qquad (2.13)$$

which can be evaluated explicitly:

$$g_G(\varepsilon) = g_0 \mathscr{G}(\varepsilon, \Delta)\Theta(\varepsilon - \Delta). \qquad (2.14)$$

It is interesting to notice that the low-energy limit, $\varepsilon \ll \Delta$, of $g_W(\varepsilon)$ reduces to the 3DD case:

$$g_W(\varepsilon \ll \Delta) = g_0 \frac{\varepsilon^2}{\sqrt{\Delta}}. \qquad (2.15)$$

The three densities of states, Eqs. (2.12), (2.14), and (2.15) are shown in Fig. 2. The DOS in Eq. (2.15) is twice the value of a single Dirac cone since in the low-energy Weyl picture, there are two equal contributions of the Weyl points to the total DOS. This can be seen from Fig. 3, where the Fermi surface is shown for the WSM and GSM scenarios. When Fermi energy is below Δ, Lifshitz transition takes place and the WSM Fermi
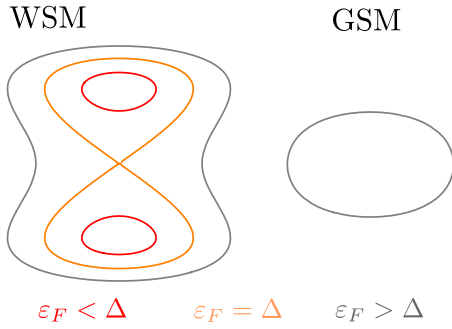
WSM   GSM

FIG. 3. The $k_y = 0$ cross section of the Fermi surface shown for the Weyl semimetal and gapped semimetal case, at different Fermi energy values. For the Weyl case, the orange curve separates the two different Fermi surface topologies. The orange line corresponds to the kink in the density of states.

surface contains two electron pockets which begin to merge at the Fermi energy $\varepsilon_F = \Delta$. This energy corresponds to the van Hove discontinuity in the DOS, seen as a kink in Fig. 2.

The DOS for the zero gap case is most easily obtained by setting $\Delta = 0$ in Eq. (2.14). This gives

$$g(\varepsilon) = g_0 \varepsilon^{3/2}. \tag{2.16}$$

Notice that the above value of the DOS is the high-energy $\varepsilon \gg \Delta$ limit of Eqs. (2.14) and (2.12).

III. ZERO-TEMPERATURE DC QUANTITIES

Having evaluated the DOS, we can proceed to calculate the often used transport quantities: the total concentration of conduction electrons n, the effective concentration of conducting electrons n_α, the resistivity ϱ_α, and the electron mobility μ_α. All calculations in this section are performed for $T = 0$ for both the GSM and WSM cases.

A. Total electron concentration n

The total carrier concentration n is defined in the usual way:

$$n = 2 \sum_{\mathbf{k}} f_{\mathbf{k}} = \int g(\varepsilon) f(\varepsilon, \mu) d\varepsilon. \tag{3.1}$$

At $T = 0$, the Fermi-Dirac function is $f(\varepsilon, \mu) = \Theta(\varepsilon_F - \varepsilon)$ and it simply modifies the upper integration limit. In integrating Eq. (3.1) with the DOS as defined in the previous section, we define a second auxiliary function $\mathcal{N}(\varepsilon, \Delta)$:

$$\mathcal{N}(\varepsilon, \Delta) = (3\varepsilon + 2\Delta)(\varepsilon - \Delta)^{3/2}. \tag{3.2}$$

In this way, we are able to write the total concentration of electrons in the GSM case as

$$n_G(\varepsilon_F) = \tfrac{2}{15} g_0 \mathcal{N}(\varepsilon_F, \Delta) \Theta(\varepsilon_F - \Delta), \tag{3.3}$$

and similarly for the WSM case:

$$\begin{aligned} n_W(\varepsilon_F) = \tfrac{2}{15} g_0 [\mathcal{N}(\varepsilon_F, -\Delta) \Theta(\varepsilon_F - \Delta) \\ + (\mathcal{N}(\varepsilon_F, -\Delta) - \mathcal{N}(-\varepsilon_F, -\Delta)) \Theta(\Delta - \varepsilon_F)]. \end{aligned} \tag{3.4}$$

The total concentration is plotted in Fig. 4(a) (full lines) for the GSM and WSM cases as a function of ε_F / Δ, in unit of concentration n_0:

$$n_0 = \tfrac{2}{15} g_0 |\Delta|^{5/2}. \tag{3.5}$$

This unit has a value of $n_0 = 3.17 \times 10^{14}$ cm^{-3} if the experimental values from Table I are used.

B. Effective electron concentration n_α

The effective concentration of the conduction electrons is a direction dependent variable defined as [29,30]

$$n_\alpha = -\frac{2}{V} \sum_{\mathbf{k}} m_e (v_{\alpha \mathbf{k}})^2 (\partial f_{\mathbf{k}} / \partial \varepsilon_{\mathbf{k}}). \tag{3.6}$$

Here, α is a Cartesian component, m_e is the electron bare mass, and $v_{\alpha \mathbf{k}} = (1/\hbar) \, \partial \varepsilon_{\mathbf{k}} / \partial k_\alpha$ is the electron group velocity.
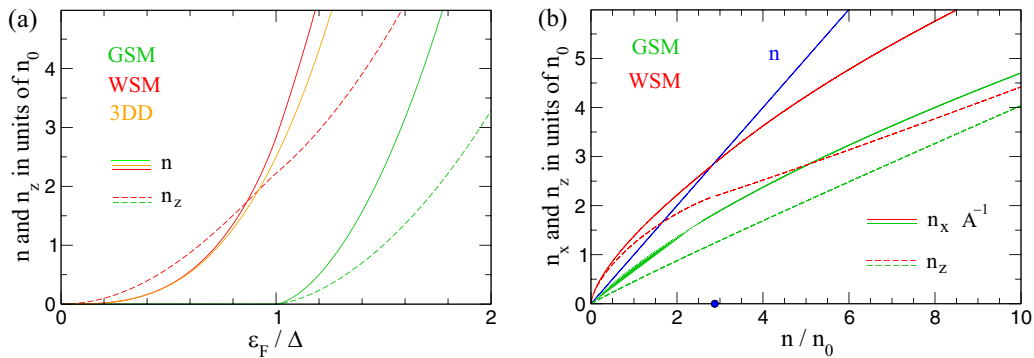

FIG. 4. (a) The total electron concentrations for the gapped semimetal, Eq. (3.3), Weyl semimetal, Eq. (3.4), and a low-energy limit of Weyl semimetal, which is a 3DD, Eq. (3.10), are shown by the full lines. For the first two cases, the effective concentration in z direction is also shown by dashed lines, as given by Eqs. (3.12) and (3.13). All concentrations are plotted in units of n_0, Eq. (3.5). (b) The effective concentration for gapped semimetal and Weyl semimetal cases, in the x and z directions, n_x and n_z, respectively, plotted as a function of the total concentration n. The n_x concentrations are multiplied by $A^{-1} \approx 0.001$ to fit into the same figure. The blue dot represents the concentration $n = 2\sqrt{2} n_0$ at which the states of the WSM are filled up to $\varepsilon_F = \Delta$, corresponding to the orange line in Fig. 3.

At $T = 0$, $\partial f_{\mathbf{k}}/\partial \varepsilon_{\mathbf{k}} = -\delta(\varepsilon_{\mathbf{k}} - \varepsilon_F)$, which excludes all states except those at the Fermi level. The expression in Eq. (3.6) forms a part of the Drude formula,

$$\sigma_\alpha(\omega) = \frac{ie^2}{m_e} \frac{n_\alpha}{\omega + i/\tau}, \qquad (3.7)$$

where n_α defines the Drude spectral weight related to the plasmon frequency, which is most easily seen in a reflectivity measurement. A common feature of the dispersions in Eq. (2.2) is the similar shape of their electron velocity in the $\alpha = (x, y)$ direction, $v_{\alpha\mathbf{k}}^\nu = \hbar v_\alpha^2 k_\alpha / \varepsilon_{\mathbf{k}}^\nu$. We have inserted this velocity in Eq. (3.6), so we can evaluate n_x^ν for GSM and WSM cases using the approach outlined in Sec. II B. The result for the GSM is

$$n_x^G(\varepsilon_F) = \frac{m_e v_x^2}{\Delta} \frac{\Delta}{\varepsilon_F} n_G(\varepsilon_F), \qquad (3.8)$$

and similarly for the WSM:

$$n_x^W(\varepsilon_F) = \frac{m_e v_x^2}{\Delta} \frac{\Delta}{\varepsilon_F} n_W(\varepsilon_F). \qquad (3.9)$$

Both concentrations, Eqs. (3.8) and (3.9), have the same high-energy limit, when $\varepsilon_F \gg \Delta$. For energies below Δ, only n_x^W remains finite,

$$n_x^W(\varepsilon_F) = \frac{2}{3\pi^2 \hbar^3} \frac{m_e v_x^2}{v_x v_y v_z} \varepsilon_F^2, \qquad (3.10)$$

and gives the same result as found for the 3DD dispersion [8,15] once we substitute Eq. (2.4) in Eq. (3.9). The $\alpha = y$ case is obtained by a simple exchange $x \to y$ in Eqs. (3.8) and (3.9).

A different behavior is anticipated for the n_z^ν, primarily because of the different velocity dependence $v_{z\mathbf{k}}^\nu = 2\hbar c^2 k_z (\hbar^2 c^2 k_z^2 + \nu\Delta)/\varepsilon_{\mathbf{k}}^\nu$. Solving for n_z calls for the definition of yet another auxiliary function,

$$\mathcal{M}(\varepsilon, \Delta) = (15\varepsilon^2 + 12\varepsilon\Delta + 8\Delta^2)(\varepsilon - \Delta)^{3/2}, \qquad (3.11)$$

which then yields

$$n_z^G(\varepsilon_F) = \frac{4}{105} g_0 \frac{m_e c^2}{\varepsilon_F} \mathcal{M}(\varepsilon_F, \Delta)\Theta(\varepsilon_F - \Delta), \qquad (3.12)$$

and

$$\begin{aligned} n_z^W(\varepsilon_F) = \frac{4}{105} g_0 \frac{m_e c^2}{\varepsilon_F} [\mathcal{M}(\varepsilon_F, -\Delta)\Theta(\varepsilon_F - \Delta) \\ + (\mathcal{M}(\varepsilon_F, -\Delta) - \mathcal{M}(-\varepsilon_F, -\Delta))\Theta(\Delta - \varepsilon_F)]. \end{aligned} \qquad (3.13)$$

From Table I, we see that $m_e c^2 = 1/4$, allowing us to plot both concentrations, Eqs. (3.12) and (3.13), in Fig. 4(a) in units of n_0 as a function of the ratio ε_F/Δ. What we see from Fig. 4(a) is that both the total and the effective electron concentrations are very similar in shape for the GSM and WSM at Fermi energies above $\varepsilon_F = \Delta$, where the $n^\nu > n_z^\nu$. This trend is reversed for low Fermi energies, $\varepsilon_F < \Delta$, where only the WSM concentrations remain finite. In addition, the effective electron concentration for the Weyl case, Eq. (3.13), has a weak hump at $\varepsilon_F = \Delta$. This is produced by a kink in the DOS. The effective concentrations for the gapped, Eq. (3.8),

and the Weyl case, Eq. (3.9), in comparison to the total carrier concentrations, Eqs. (3.3) and (3.4), are $A = m_e v_x^2/\Delta = 930$ times larger if we take the values from the Table I. The parameter A is used in plotting the concentrations in Fig. 4(b). Experimentally, it is natural to express the transport quantities as functions of the doping or the total carrier concentration n. This procedure is carried out numerically by expressing ε_F/Δ as a function of the total concentration, Eq. (3.3) for the WSM and Eq. (3.4) for the GSM, and then inserting this into the effective concentrations, Eqs. (3.8) through (3.13).

Figure 4(b) shows the effective GSM and WSM carrier concentrations, n_α^ν, as a function of the total carrier concentration n^ν. The WSM case (red lines) is visibly different form the GSM case (green lines). Through this difference we might obtain insight on how to distinguish the GSM case from the WSM case, at zero temperature, based on the resistivity anisotropy. This is done in the following section.

The zero gap case follows trivially from Eq. (3.3) which, after setting $\Delta = 0$, gives the total concentration:

$$n(\varepsilon_F) = \frac{2}{5} g_0 \varepsilon_F^{5/2}. \qquad (3.14)$$

Setting $\Delta = 0$ may also be applied to all other effective concentrations.

C. Mobility and resistivity

The conduction electron mobility μ is defined through the following relation [31]:

$$\sigma_\alpha^\nu(0) = e\mu_\alpha^\nu n^\nu. \qquad (3.15)$$

Through comparison with Eq. (3.7), we conclude

$$\mu_\alpha^\nu = \frac{e\tau}{m_e} \frac{n_\alpha^\nu}{n^\nu}. \qquad (3.16)$$

Based on the results for WSM and GSM cases for in-plane effective concentrations, $\alpha = (x, y)$, we have

$$\mu_\alpha^\nu = \frac{e\tau}{m_e} \frac{m_e v_\alpha^2}{\Delta} \frac{\Delta}{\varepsilon_F}. \qquad (3.17)$$

The large ratio $A = 930$ is key in the above expression, meaning that a very large intralayer carrier mobility in ZrTe$_5$, reaching up to 0.45×10^6 cm^2/(Vs), is related to a high Fermi velocity (Table I).

For the z direction, the limit of $\varepsilon_F \gg \Delta$ gives the identical mobility for the WSM and GSM cases:

$$\mu_z^\nu = \frac{5}{14} \frac{e\tau}{m_e}. \qquad (3.18)$$

For the GSM, $\mu_z^G = 2ec^2\tau = e\tau/m^*$ when the Fermi level ε_F hits just above Δ. This is a usual result for a paraboliclike dispersion with an effective mass m^*, but interestingly it comes with a different numerical prefactor than the high-energy limit of carrier mobility [Eq. (3.18)]. The $\varepsilon_F \ll \Delta$ WSM case is

$$\mu_z = \frac{e\tau}{m_e} \frac{\Delta}{\varepsilon_F}, \qquad (3.19)$$

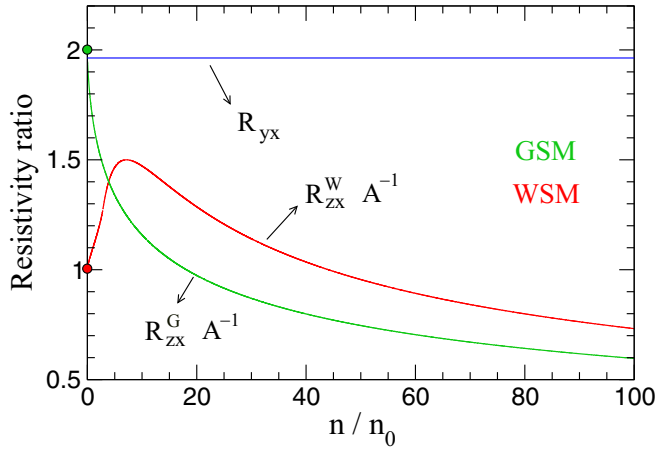which is equivalent to Eq. (3.17) once we use the substitution in Eq. (2.4).

FIG. 5. Resistivity anisotropy defined as $R_{\alpha\beta} = \varrho_\alpha/\varrho_\beta$ and evaluated at $T = 0$ as a function of total carrier concentration for gapped semimetal and Weyl semimetal cases. While R_{xy} is constant, R_{zx}^G strongly increases at low carrier concentration and R_{zx}^W has a peak. Note that R_{zx}^G and R_{zx}^W are scaled down by a factor of $1/A = 1/930$.

The direction-dependent resistivity anisotropy is best seen through the resistivity ratio $R_{\alpha\beta}$, where $(\alpha, \beta) \in (x, y, z)$ defined from the Drude formula [Eq. (3.7)] for the GSM and WSM cases:

$$R_{\alpha\beta}^v = \frac{\varrho_\alpha^v}{\varrho_\beta^v} = \frac{n_\beta^v}{n_\alpha^v}. \tag{3.20}$$

The in-plane resistivity ratio is straightforward and equal for the GSM and WSM cases. Using Eqs. (3.8), (3.9), and Table I, we get

$$R_{yx} = v_x^2/v_y^2 = 1.96. \tag{3.21}$$

This constant value is shown in Fig. 5 in blue, and it is very close to the experimentally obtained value $R_{yx}^{\text{expt}} \approx 2$ [14].

In contrast to Eq. (3.21), the out-of-plane anisotropy R_{zx} strongly depends on the total concentration of electrons n. This is seen in Fig. 5 where R_{zx} is plotted for the WSM and GSM cases as a function of n/n_0. The upper limit of the plot is $100 n_0$. For $\Delta = 3$ meV (Table I), this corresponds to a Fermi energy of $\varepsilon_F^G = 13.4$ meV [Eq. (3.3)] in the GSM and $\varepsilon_F^W = 11.4$ meV [Eq. (3.4)] in the WSM case. In the low-concentration limit, R_{zx}^G and R_{zx}^W are visibly different. While R_{zx}^G decreases monotonically from the maximal value of $2A$; R_{zx}^W increases to a maximum located at $7.3 n_0$, only to start decreasing for larger doping. This qualitatively different behavior of R_{zx} as a function of n is the key to distinguish the GMS from the WSM in DC transport, under the condition that the samples can be chemically or electrostatically doped. Experimentally, one can measure the anisotropy R_{zx}, for example, using microfabricated samples [14]. Using expressions for effective carrier concentrations, Eqs. (3.7)–(3.9) gives in the high concentration limit $n \gg n_0$:

$$R_{zx}^v \approx \frac{14}{5} \frac{m_e v_x^2}{\Delta} \left[\left(\frac{n}{3n_0} \right)^{2/5} + v\frac{2}{15} \right]^{-1}. \tag{3.22}$$

This is shown in Fig. 5, where the splitting between the GSM and WSM follows from Eq. (3.22). In the opposite,

low-energy limit when $\varepsilon_F \ll \Delta$, the resistivity anisotropy is only meaningful in the WSM case where it is given by

$$R_{zx}^W \approx \frac{v_x^2}{v_z^2}. \tag{3.23}$$

The resistivity anisotropies containing z and y directions follow analogously.

In the zero-gap case, R_{yx} is the same as Eq. (3.21), while R_{zx} is

$$R_{zx} = \frac{14}{5} \frac{m_e v_x^2}{\varepsilon_F} \propto n^{-2/5}, \tag{3.24}$$

an exact result over the entire range of concentration n. Contrary to the GSM and WSM cases, both of which have finite values in the $n \to 0$ limit as seen in Fig. 5, the zero gap resistivity anisotropy, Eq. (3.24), diverges for small concentrations. This makes it a valuable indicator about the possible nature of the ground state.

IV. OPTICAL CONDUCTIVITY

When dealing with the optical response of an insulator or a semimetal, we normally use a conductivity formula containing a phenomenological interband relaxation rate Γ. This interband Γ is different from the intraband or Drude relaxation rate $1/\tau$. In the two-band model, the interband conductivity is [32]

$$\text{Re}\,\sigma_\alpha(\Omega, T) = \frac{2i\hbar}{V} \sum_{\mathbf{k}} \frac{\left| J_{\alpha\mathbf{k}}^{vc} \right|^2}{\varepsilon_{\mathbf{k}}^c - \varepsilon_{\mathbf{k}}^v} \frac{f_{\mathbf{k}}^v - f_{\mathbf{k}}^c}{\Omega - \varepsilon_{\mathbf{k}}^c - \varepsilon_{\mathbf{k}}^v + i\Gamma} + c \leftrightharpoons v. \tag{4.1}$$

In Eq. (4.1), we introduced $\Omega = \hbar\omega$ and the α-dependent interband current vertices $J_{\alpha\mathbf{k}}^{vc}$ [33] which are calculated in the Appendix for the WSM and GSM cases. Here we limit our discussion to the interband conductivity, knowing that a Drude term will always be present for a finite carrier density.

We analytically evaluate the real part of the conductivity tensor [Eq. (4.1)] in the limit $\Gamma \to 0$. Considering only $\Omega > 0$, the above expression Eq. (4.1) becomes

$$\text{Re}\,\sigma_\alpha(\Omega, T) = \frac{2\hbar\pi}{V} \sum_{\mathbf{k}} \left| J_{\alpha\mathbf{k}}^{vc} \right|^2 \frac{f_{\mathbf{k}}^v - f_{\mathbf{k}}^c}{\varepsilon_{\mathbf{k}}^c - \varepsilon_{\mathbf{k}}^v} \delta\left(\Omega - \varepsilon_{\mathbf{k}}^c + \varepsilon_{\mathbf{k}}^v \right). \tag{4.2}$$

The Fermi-Dirac distributions in the above expression are simplified by taking into account the symmetry of the bands $\varepsilon_{\mathbf{k}}^c = -\varepsilon_{\mathbf{k}}^v$ and the fact that the expression Eq. (4.2) is finite only for $\Omega = \varepsilon_{\mathbf{k}}^c - \varepsilon_{\mathbf{k}}^v$. We can then write the distribution function as

$$\mathscr{F}(\Omega, T) = f_{\mathbf{k}}^v - f_{\mathbf{k}}^c = \frac{\sinh(\beta\Omega/2)}{\cosh(\beta\mu) + \cosh(\beta\Omega/2)}. \tag{4.3}$$

In the $T = 0$ case, the above expression simplifies to $\mathscr{F}(\Omega, 0) = \Theta(\Omega - 2\varepsilon_F)$, which describes the suppression of the interband transitions due to the Pauli blocking.

Calculation of $\text{Re}\,\sigma_x(\Omega, T)$ follows analogously to the procedure outlined in previous sections. First we insert the interband current vertex, Eq. (A9), into Eq. (4.2). The new variables are $2\hbar v_x k_x = x$, $2\hbar v_y k_y = y$ and $\sqrt{2}\hbar c k_z = z$. After
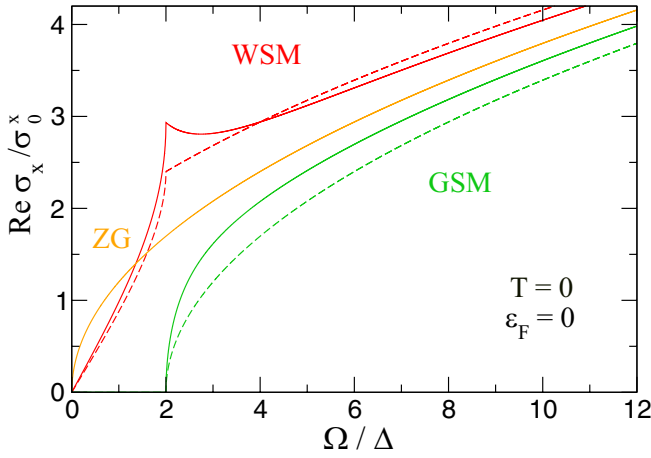
FIG. 6. The optical conductivity of gapped semimetal [Eq. (4.8)] and Weyl semimetal [Eq. (4.14)] are plotted in full lines in the case of $\varepsilon_F = 0$ in units of σ_0^x. The dashed lines represent the optical conductivity at zero ε_F, but using the approximate expression Eq. (4.6) within Eqs. (4.8) and (4.14). The zero gap (ZG) phase optical conductivity [Eq. (4.18)] is shown in orange.

the transformation into the cylindrical system, we have

$$\mathrm{Re}\,\sigma_x^y(\Omega, T) = \frac{1}{16\sqrt{2}\pi}\frac{e^2}{\hbar^2}\frac{v_x^2}{v_x v_y c}\frac{\mathscr{F}(\Omega, T)}{\Omega}\int \varrho\, d\varrho \int dz$$
$$\times \delta(\Omega - \sqrt{\varrho^2 + (z^2 + \nu 2\Delta)^2})$$
$$\times \left(1 + \frac{(z^2 + \nu 2\Delta)^2}{\Omega^2}\right). \quad (4.4)$$

The solution to Eq. (4.4) will be facilitated by introducing yet another auxiliary function:

$$\mathscr{D}(\Omega, \Delta) = \sqrt{\Omega - 2\Delta}\left(1 + \frac{3\Omega^2 + 8\Delta\Omega + 32\Delta^2}{15\Omega^2}\right). \quad (4.5)$$

Here we mention briefly some of the properties of $\mathscr{D}(\Omega, \Delta)$. For Ω just above 2Δ, Eq. (4.5) reduces to $\mathscr{D}(\Omega, \Delta) \approx 2\sqrt{\Omega - 2\Delta}$. In the opposite limit ($\Omega \gg \Delta$), we have $\mathscr{D}(\Omega, \Delta) \approx (6/5)\sqrt{\Omega}$. In all cases of interest, function $\mathscr{D}(\Omega, \Delta)$ can be well enough approximated by

$$\mathscr{D}(\Omega, \Delta) \approx (6/5)\sqrt{\Omega - 2\Delta}. \quad (4.6)$$

To simplify our optical expressions, we define the units of conductivity, σ_0^α. They depend on the component $\alpha \in (x, y, z)$:

$$\sigma_0^\alpha = \frac{e^2}{8\sqrt{2}\pi\hbar^2}\frac{1}{v_x v_y c}\left(v_x^2\delta_{\alpha,x} + v_y^2\delta_{\alpha,y} + 2c^2\delta_{\alpha,z}\right). \quad (4.7)$$

In continuation, we determine the optical conductivities separately for the GSM and WSM cases.

A. Optical conductivity for gapped semimetal case

The real part of the x component of the interband conductivity is given for the GSM ($\nu = +1$) case by

$$\mathrm{Re}\,\sigma_x^G(\Omega, T) = \sigma_0^x\mathscr{F}(\Omega, T)\mathscr{D}(\Omega, \Delta). \quad (4.8)$$

Figure 6 shows the optical conductivity determined from Eq. (4.8) for the intrinsic case where $\varepsilon_F = 0$, in other

words $\mathscr{F}(\Omega, T) = 1$. If an approximate expression shown in Eq. (4.6) is used in Eq. (4.8), it leads to a simplified version of the interband conductivity:

$$\mathrm{Re}\,\sigma_x^G(\Omega, T = 0) \approx \sigma_0^x\frac{6}{5}\sqrt{\Omega - 2\Delta}\,\Theta(\Omega - 2\varepsilon_F). \quad (4.9)$$

This approximate result is also shown in Fig. 6 with a dashed line, and it is rather close to the exact expression in Eq. (4.8).

Figure 7 shows the real part of the optical conductivity determined from Eq. (4.8) for various temperatures given in units of Fermi temperature, $k_B T_F = \varepsilon_F$. We consider two cases. In the first case, we neglect the temperature variation of the electron chemical potential by fixing $\varepsilon_F = \mu(T = 0)$. In the second case, we include the temperature dependence of the chemical potential $\mu(T)$, and we calculate $\mu(T)$ self-consistently from the relation Eq. (3.1) inserted into Eq. (4.3). The difference between using $\mu(T)$ or ε_F diminishes at $T \ll T_F$, and at high temperatures, $T > T_F$. The reason for this is that at low temperatures $\mu \approx \varepsilon_F$, and at high temperatures the Fermi-Dirac distribution is smeared beyond the temperature dependence of $\mu(T)$. Interestingly, in the intermediate temperature range where $T \sim T_F$, the optical conductivity develops a linear-like energy dependence. This quasilinear optical response of $\mathrm{Re}\,\sigma_x^G(\Omega, T > T_F)$ shown in Fig. 7 can easily be mistaken for a sign of a 3DD-like band structure. In fact, the apparent linearity only represents a crossover regime between the low-temperature convex and the high-temperature concave behavior of optical conductivity. Such progression of the optical conductivity from low to high temperatures can be seen in experiments, for example in Fig. 2(d) of Ref. [9].

The derivation of $\mathrm{Re}\,\sigma_y^G(\Omega)$ is essentially the same, the only difference arising from the current vertex which changes the ratio of the electronic velocities. The resulting real part of the optical conductivity is

$$\mathrm{Re}\,\sigma_y^G(\Omega, T) = \sigma_0^y\mathscr{D}(\Omega, \Delta)\mathscr{F}(\Omega, T). \quad (4.10)$$

The differences are, just like in the DC transport, addressed in Sec. III, in the z direction. This is a result of a different current vertex $J_{z\mathbf{k}}^{vc}$ [Eq. (A10)]. Introducing the fifth and final auxiliary function $\mathscr{Z}(\Omega, \Delta)$,

$$\mathscr{Z}(\Omega) = \frac{8}{105}\frac{1}{\Omega^2}\sqrt{\Omega - 2\Delta}\,(\Omega - 2\Delta)^2(5\Omega + 2\Delta), \quad (4.11)$$

we can write the z component of the optical conductivity in a more compact way:

$$\mathrm{Re}\,\sigma_z^G(\Omega, T) = \sigma_0^z\mathscr{F}(\Omega, T)\mathscr{Z}(\Omega, \Delta). \quad (4.12)$$

Energy properties of Eq. (4.12) are determined by the function $\mathscr{Z}(\Omega, \Delta)$, whose limit $\mathscr{Z}(\Omega \gg 2\Delta, \Delta) \sim \Omega^{3/2}$ determines the high-energy z components of the real part of the conductivity:

$$\mathrm{Re}\,\sigma_z^G(\Omega, T) \propto \Omega^{3/2}. \quad (4.13)$$

This function is plotted in Fig. 8 and is visibly different from the xy plane conductivity [Fig. 7(a)], which behaves as $\propto \Omega^{1/2}$. However, the z-axis optical conductivity is experimentally much less accessible due to the sample morphology. No reflective surface of single crystals of $ZrTe_5$ contains the z axis.
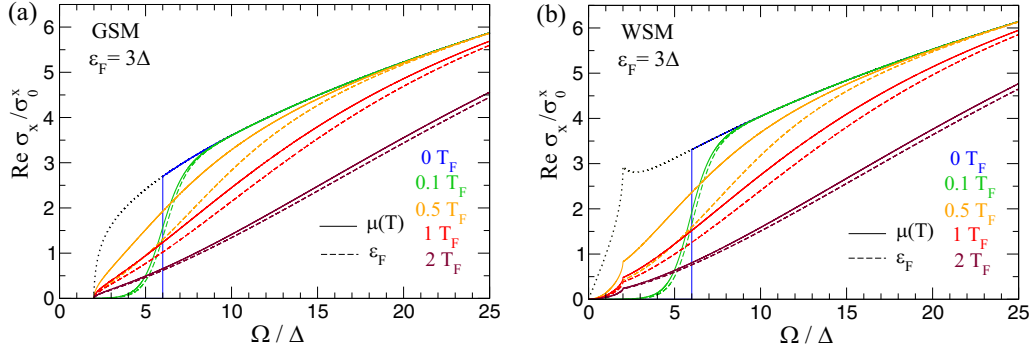
FIG. 7. The x component of the real part of the optical conductivity is shown for (a) the gapped semimetal [Eq. (4.8)] is and (b) the Weyl semimetal [Eq. (4.14)]. The optical conductivity is shown at various temperatures. Both conductivities are given in units of σ_0^x, as a function of Ω which is scaled to the gap parameter Δ for a particular value of Fermi energy, $\varepsilon_F = 3\Delta$. The full lines are optical conductivity calculated using $\mu(T)$, while the dashed lines are calculated using constant $\mu(T) = \mu(0) = \varepsilon_F$. The $\mathscr{F}(\Omega, T) = 1$ case is represented by dotted lines in both panels.

B. Optical conductivity for Weyl semimetal case

Similar analysis applies to the WSM case. Once again, using the shorthand introduced in Eq. (4.5), the real component of the optical conductivity along x axis is

$$\mathrm{Re}\,\sigma_x^W(\Omega, T) = \sigma_0^x \mathscr{F}(\Omega, T)[\mathscr{D}(\Omega, -\Delta)\Theta(\Omega - 2\Delta) \\ + (\mathscr{D}(\Omega, -\Delta) - \mathscr{D}(-\Omega, -\Delta))\Theta(2\Delta - \Omega)].$$
(4.14)

The basic features of this function are displayed in Fig. 6, where Eq. (4.14) is plotted for the case that $\mathscr{F}(\Omega, T) = 1$ and taking the full expression Eq. (4.5), shown in a full line, versus the approximation Eq. (4.6), shown in a dashed line. The linearity of $\mathrm{Re}\,\sigma_x^W(\Omega, T)$ is clearly seen for $\Omega < 2\Delta$. By expanding Eq. (4.14) for small energies Ω, we have indeed,

$$\mathrm{Re}\,\sigma_x^W(\Omega \ll 2\Delta, T) \approx \frac{e^2}{6\pi \hbar^2} \frac{v_x^2}{v_x v_y v_z} \Omega \, \mathscr{F}(\Omega, T),$$
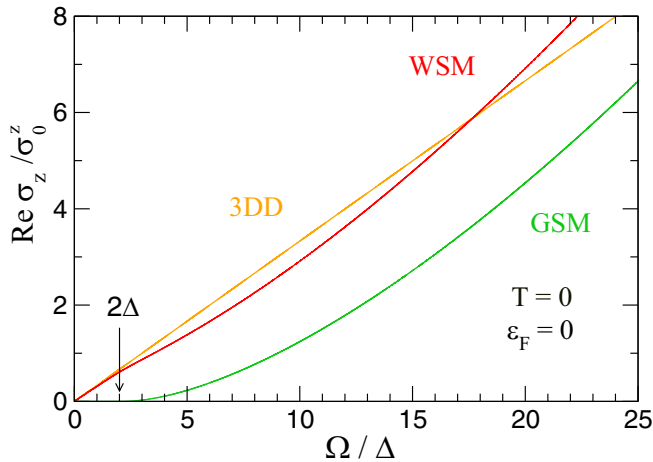(4.15)

FIG. 8. The real part of the optical conductivity as calculated in the z direction for gapped semimetal, Eq. (4.12), and Weyl semimetal case, Eq. (4.17), plotted in units of σ_0^z. The 3DD dispersion case, Eq. (4.15), is added for comparison.

in accordance with the 3DD spectrum [8]. At the energy $\Omega = 2\Delta$, a direct transition between two hyperbolic points in the energies of Eq. (2.2) occurs, and manifests itself as a kink in the curve, just as it did in the DOS. In the case of $\Omega \gg 2\Delta$, the optical conductivity becomes

$$\mathrm{Re}\,\sigma_x^W(\Omega, T = 0) \approx \sigma_0^x \frac{6}{5}\sqrt{\Omega + 2\Delta}\,\Theta(\Omega - 2\varepsilon_F). \quad (4.16)$$

Figure 7(b) shows the WSM optical conductivity from Eq. (4.14) plotted for various temperatures T_F. As in the previous calculation, the case of constant $\varepsilon_F = \mu(T = 0)$ and the $\mu(T)$ have been addressed. The $\mu(T)$ was calculated self-consistently from Eq. (3.1). In addition to the similar temperature-dependent features like in the GSM case, we see a persistent kink at 2Δ at all temperatures. This kink comes from the merging of the Weyl cones and the related direct transitions between van Hove points.

The z component is

$$\mathrm{Re}\,\sigma_z^W(\Omega, T) \\ = \sigma_0^z \mathscr{F}(\Omega, T)[\mathscr{Z}(\Omega, -\Delta)\Theta(\Omega - 2\Delta) \\ + (\mathscr{Z}(\Omega, -\Delta) - \mathscr{Z}(-\Omega, -\Delta))\Theta(2\Delta - \Omega)], \quad (4.17)$$

with the $\mathrm{Re}\,\sigma_z(\Omega, T) \propto \Omega^{3/2}$ in the high Ω limit, like for the GSM in Eq. (4.13). In the low-energy limit, the above relation, Eq. (4.17), reduces to the expression in Eq. (4.15), with v_x replaced by v_z.

C. Optical conductivity for zero gap case

In the zero gap phase, the GSM and WSM expressions from the previous two sections reduce to the same result. Since $\mathscr{D}(\Omega, \Delta = 0) = (6/5)\sqrt{\Omega}$, for the $\alpha = x, y$ components of the conductivity, we get

$$\mathrm{Re}\,\sigma_\alpha(\Omega, T) = \sigma_0^\alpha \frac{6}{5}\sqrt{\Omega}\,\mathscr{F}(\Omega, T). \quad (4.18)$$

The above conductivity is shown in Fig. 6. In a similar way, the z component of the real part of the optical conductivity is obtained by setting $\Delta = 0$ in Eq. (4.12), which makes Eq. (4.13) an exact result.

D. Optical conductivity anisotropy

The ratio of the x [Eq. (4.8)] and y [Eq. (4.10)] components of the real part of the optical conductivity is very much analogous to the analysis followed in Sec. III C. For both the GSM and WSM, the optical conductivity anisotropy is identical,

$$\frac{\operatorname{Re}\sigma_x^\nu(\Omega, T)}{\operatorname{Re}\sigma_y^\nu(\Omega, T)} = \frac{v_x^2}{v_y^2}, \qquad (4.19)$$

and given by an expression analogous to the resistivity anisotropy in Eq. (3.20). For the majority of anisotropic Dirac systems, the velocity ratio is $v_x/v_y \sim 1$ [34–36], and ZrTe$_5$ is no exception with its $v_x/v_y = 1.4$. In some systems, this ratio was reported to be an order of magnitude larger [37]. Another equally important parameter responsible for the amplitude of the optical conductivity is the effective mass m^*, hidden in v_z [Eq. (2.4)], which should be very large, $m^* \gg m_e$ for the model described in Eq. (2.1) to be applicable. The effective mass m^* plays a role in the following ratio which involves the z-component conductivity:

$$\frac{\operatorname{Re}\sigma_z^\nu(\Omega, T)}{\operatorname{Re}\sigma_x^\nu(\Omega, T)} \approx \frac{2}{3}\frac{\Delta}{m^* v_x^2}\left(\frac{\Omega}{2\Delta} - \nu\right). \qquad (4.20)$$

Similar to the DC case [Eq. (3.22)], because of the very large characteristic energy $m^* v_x^2 \gg 1$ eV, the above ratio is extremely small in the energy range where the model [Eq. (2.1)] is valid.

It is worth mentioning that $\operatorname{Re}\sigma_{x,y}^\nu$ are nicely described by the approximative function, Eq. (4.6), compared to the exact one in Eq. (4.5), as can be seen from Fig. 6. If we go back to Sec. II B, we may notice that $\operatorname{Re}\sigma_{x,y}^\nu$ with Eq. (4.6) is in fact proportional to $g_\nu(\Omega, 2\Delta)/\Omega$. This is in accordance with the usual rule-of-thumb derivation of the optical conductivity [30], where the interband current vertex is assumed to be a constant in Eq. (A11). While this simplification works well for the (x, y) case, it utterly fails for the z direction [see Eq. (A10)].

We emphasize that our model, Eq. (2.1), is restricted in calculating the optical response of the ZrTe$_5$. As previously stated, experimental data agrees with the predictions of Eq. (4.9) up to photon energy $\hbar\omega \approx 120$ meV. The upper Pauli edge given by Eq. (4.3) is twice the critical Fermi energy ε_F^c. Below the energy ε_F^c, the electron dispersions are indeed given by Eq. (2.2). Since we take $\Delta = 3$ meV in the calculations in this section, the results in Fig. (6)–(8) fall well into the interval of the model's applicability. The problem lies in the results for WSM and GSM optical conductivity for energies larger than 2Δ. They both have a similar $\sim\omega^{1/2}$ dependence. This similarity makes it difficult to distinguish between the two cases, unless the Pauli edge is very low, less than 2Δ. For such a low Pauli edge—which corresponds to a very low impurity doping—one could detect the kink in the optical response, if ZrTe$_5$ was a WSM.

E. Finite interband relaxation rate Γ and finite temperature effects in the GSM case

Finite interband relaxation Γ contribution to the $\operatorname{Re}\sigma_x(\Omega, T)$ is calculated numerically from the expression Eq. (4.2). Finite Γ modifies the onset of the single-particle
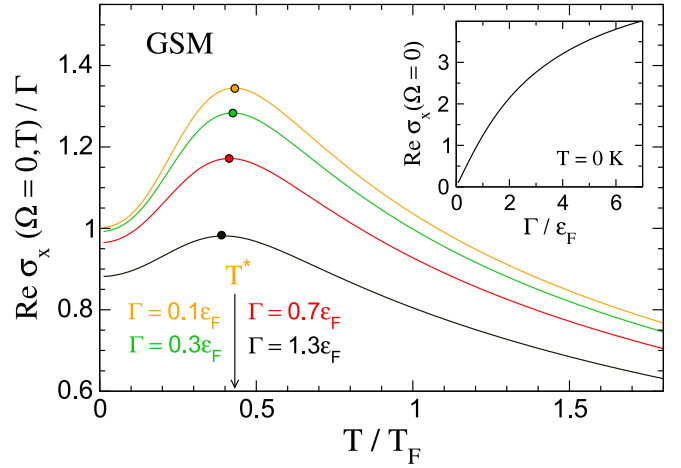

FIG. 9. Real part of the static interband conductivity, $\operatorname{Re}\sigma_x^G(\Omega = 0, T)/\Gamma$, as a function of temperature T, plotted for several values of interband relaxation Γ. The maximum located at T^* (colored circles) slowly shifts to lower values with increasing Γ. The inset of the picture shows $\operatorname{Re}\sigma_x^G(\Omega = 0)$ as a function of Γ/ε_F at $T = 0$.

excitation in comparison with the analytical result in Eq. (4.4), which then gives a nonzero value of the static interband conductivity $\operatorname{Re}\sigma_x(0, 0)$ in the band gap region, even at zero temperatures.

The increase of the static interband conductivity can be clearly seen in the inset of Fig. 9, where $\operatorname{Re}\sigma_x^G(0)$ is shown as a function of Γ. Deriving this functional dependence is straightforward in the case of a 3DD dispersion [15]. In the GSM case, we can find the result numerically:

$$\operatorname{Re}\sigma_x(0, 0) \propto \sqrt{\Gamma}\arctan\left(\sqrt{\Gamma/2\varepsilon_F}\right). \qquad (4.21)$$

The above expression shows a linear increase of the $\Omega = 0$ interband conductivity for the interband damping $\Gamma < \varepsilon_F$, and a stronger deviation for higher values of Γ.

The temperature dependence of $\operatorname{Re}\sigma_x^G(\Omega = 0, T)/\Gamma$ is plotted in Fig. 9 for various values of the interband relaxation Γ. The strong increase of the static $T = 0$ value of the conductivity is noteworthy. This has already been addressed and is shown in the inset of Fig. 9. At finite temperatures, there is a maximum located at $T^* \approx 0.4\,T_F$, which can be traced back to the smearing of the Fermi-Dirac function with increasing T. The maximum T^* slowly shifts toward lower values as we increase Γ.

This calculation is also relevant in the intrinsic case, when $\varepsilon_F = 0$. In the absence of a Drude component, the interband contribution will then dominate the response. We emphasize that the Drude component is not considered anywhere in Sec. IV, although it is present and may be large at finite temperatures or finite carrier densities.

V. CONCLUSIONS

In this paper, we have addressed the static and dynamic transport properties of the Weyl and GSM described by an effective two-band model of the valence electrons. The model implements a linear dispersion in the in-plane directions and a parabolic dispersion in the out-of-plane direction, coupled to a positive band gap in the gapped case or a negative band

gap in the Weyl case. The transport properties in the static limit, such as the direction dependent resistivity and mobility, are predominantly influenced by large values of intralayer electron velocities. The transport properties are similar in the Weyl and gapped cases at high values of Fermi energy. For energies lower than the band gap, only the Weyl phase has a finite contribution, and this limit corresponds to the well-known 3DD dispersion case.

In the limit of low concentrations, we show how to distinguish between Weyl phase, finite gap, or zero gap phase, using resistivity anisotropy in the out-of-plane direction.

The interband conductivity shows a $\omega^{1/2}$ dependence on photon energy in the in plane and a $\omega^{3/2}$ dependence in the out-of-plane direction for both GSM and WSM cases. The model predicts that the in-plane conductivity anisotropy is equal to the squared Fermi velocity ratio, just like it is the case for the DC transport. The model also shows out-of-plane conductivity anisotropy, although proportional to ω, is insignificantly small due to the comparatively large velocity v_x, within the energy interval where the two-band model applies. The effects of a finite interband relaxation constant give a finite contribution to the interband conductivity as well as a maximum in temperature at T^*, associated with the smearing of the Fermi-Dirac distribution at high temperatures and small Fermi energies.

Finally, we showed that it is not possible to distinguish WSM and GSM at higher temperatures and/or higher carrier concentrations, within our effective model. At high temperatures, both of these cases strongly resemble 3DD semimetal. This means that the measurement of optical conductivity alone should not be used to classify the topological nature of the ground state if $\varepsilon_F > 2\Delta$ at zero temperature. A similar conclusion is valid for DC transport. If the doping is high, there is no way to distinguish between WSM and GSM.

At very low doping, DC transport gives different ratios of the interlayer and intralayer resistivities for the gapped and Weyl cases. In the case of ZrTe$_5$, it remains an experimental challenge how to reach such low carrier concentrations.

Note added: Recently, we became aware of the work of Wang and Li [38], whose results are in agreement with our findings for $T = 0$ interband conductivity of our model.

APPENDIX: CURRENT VERTICIES

In the general form of the 2×2 Hamiltonian,

$$H = \begin{pmatrix} b_\mathbf{k} & a_\mathbf{k} \\ a_\mathbf{k}^* & d_\mathbf{k} \end{pmatrix}, \tag{A1}$$

the interband $L \neq \underline{L}$ current vertices can be shown to be [33]

$$J_{\alpha\mathbf{k}}^{L\underline{L}} = \sum_{\ell\ell'} \frac{e}{\hbar} \frac{\partial H_\mathbf{k}^{\ell\ell'}}{\partial k_\alpha} U_\mathbf{k}(\ell, L) U_\mathbf{k}^*(\ell', \underline{L}), \tag{A2}$$

where $U_\mathbf{k}(\ell, L)$ are the elements of unitary matrix defined as $\mathbf{U}\hat{H}\mathbf{U}^{-1} = \mathbf{E}$,

$$U_\mathbf{k}(\ell, L) = \begin{pmatrix} e^{i\varphi_\mathbf{k}} \cos(\vartheta_\mathbf{k}/2) & e^{i\varphi_\mathbf{k}} \sin(\vartheta_\mathbf{k}/2) \\ -\sin(\vartheta_\mathbf{k}/2) & \cos(\vartheta_\mathbf{k}/2) \end{pmatrix}, \tag{A3}$$

with the definitions

$$a_\mathbf{k} = |a_\mathbf{k}|e^{i\varphi_\mathbf{k}}, \quad \tan\varphi_\mathbf{k} = \frac{\mathrm{Im}\, a_\mathbf{k}}{\mathrm{Re}\, a_\mathbf{k}}, \quad \tan\vartheta_\mathbf{k} = \frac{2|a_\mathbf{k}|}{b_\mathbf{k} - d_\mathbf{k}}. \tag{A4}$$

Therefore, in the general case of Eq. (A1), Eq. (A2) gives

$$\frac{\hbar}{e} J_{\alpha\mathbf{k}}^{vc} = \frac{\tan\vartheta_\mathbf{k}}{2\sqrt{1 + \tan^2\vartheta_\mathbf{k}}} \frac{\partial(b_\mathbf{k} - d_\mathbf{k})}{\partial k_\alpha}$$
$$+ i|a_\mathbf{k}|\frac{\partial\varphi_\mathbf{k}}{\partial k_\alpha} + \frac{1}{\sqrt{1 + \tan^2\vartheta_\mathbf{k}}} \frac{\partial|a_\mathbf{k}|}{\partial k_\alpha}. \tag{A5}$$

Now we can determine the above derivations for the Hamiltonian in Eq. (2.1). We obtain

$$\frac{\partial|a_\mathbf{k}|}{\partial k_\alpha} = \hbar \frac{v_x^2 k_x \delta_{\alpha,x} + v_y^2 k_y \delta_{\alpha,y}}{\sqrt{(v_x k_x)^2 + (v_y k_y)^2}} \frac{\hbar^2 c^2 k_z^2 + \nu\Delta}{|\varepsilon_\mathbf{k}^v|} \tag{A6}$$

and

$$\frac{\partial\varphi_\mathbf{k}}{\partial k_\alpha} = \frac{v_x v_y(k_x \delta_{\alpha,y} - k_y \delta_{\alpha,x})}{(v_x k_x)^2 + (v_y k_y)^2}, \tag{A7}$$

and, trivially,

$$\frac{\partial(b_\mathbf{k} - d_\mathbf{k})}{\partial k_\alpha} = 4\hbar^2 c^2 k_z \delta_{\alpha,z}. \tag{A8}$$

In the specific case of ν for the x component of Eq. (A5),

$$\frac{\hbar^2}{e^2}|J_{x\mathbf{k}}^{vc}|^2 = \frac{\hbar^2 v_x^2}{(v_x k_x)^2 + (v_y k_y)^2}$$
$$\times \left(v_y^2 k_y^2 + v_x^2 k_x^2 \frac{(\hbar^2 c^2 k_z^2 + \nu\Delta)^2}{|\varepsilon_\mathbf{k}^v|^2} \right), \tag{A9}$$

and analogously for the $\alpha = y$ component. The z component is rather different from Eq. (A9) and is

$$\frac{\hbar^2}{e^2}|J_{z\mathbf{k}}^{vc}|^2 = 4\hbar^4 c^4 k_z^2 \frac{(\hbar v_x k_x)^2 + (\hbar v_y k_y)^2}{|\varepsilon_\mathbf{k}^v|^2}. \tag{A10}$$

In the close vicinity of the Γ point in the Brillouin zone $(k_x, k_y, k_z) \to 0$, and thus $\tan\vartheta_\mathbf{k} \to 0/\Delta = 0$. Then, inserting Eq. (A6) in Eq. (A5) for $\alpha = x, y$ we have

$$|J_{\alpha\mathbf{k}}^{vc}|^2 \approx e^2 v_\alpha^2, \tag{A11}$$

while the z component stays the same as Eq. (A10). Expanding Eqs. (A9) and (A10) around Weyl points, we again end with

$$|J_{\alpha\mathbf{k}}^{vc}|^2 = e^2 v_\alpha^2, \tag{A12}$$

where now $\alpha = (x, y, z)$ with $v_z^2 = 4\Delta c^2$.

[1] S. Okada, T. Sambongi, and M. Ido, J. Phys. Soc. Jpn. **49**, 839 (1980).

[2] T. E. Jones, W. W. Fuller, T. J. Wieting, and F. Levy, Solid State Commun. **42**, 793 (1982).

[3] M. H. Whangbo, F. J. DiSalvo, and R. M. Fleming, Phys. Rev. B **26**, 687 (1982).

[4] P. Shahi, D. J. Singh, J. P. Sun, L. X. Zhao, G. F. Chen, Y. Y. Lv, J. Li, J.-Q. Yan, D. G. Mandrus, and J. G. Cheng, Phys. Rev. X **8**, 021055 (2018).

[5] W. Wang, X. Zhang, H. Xu, Y. Zhao, W. Zou, L. He, and Y. Xu, Sci. Rep. **8**, 5125 (2018).

[6] Y. Zhang, C. Wang, L. Yu, G. Liu, A. Liang, J. Huang, S. Nie, X. Sun, Y. Zhang, B. Shen, J. Liu, H. Weng, L. Zhao, G. Chen, X. Jia, C. Hu, Y. Ding, W. Zhao, Q. Gao, C. Li, S. He, L. Zhao, F. Zhang, S. Zhang, F. Yang, Z. Wang, Q. Peng, X. Dai, Z. Fang, Z. Xu, C. Chen, and X. J. Zhou, Nat. Commun. **8**, 15512 (2017).

[7] X. Yuan, C. Zhang, Y. Liu, A. Narayan, C. Song, S. Shen, X. Sui, J. Xu, H. Yu, Z. An, J. Zhao, S. Sanvito, H. Yan, and F. Xiu, NPG Asia Mater. **8**, e325 (2016).

[8] P. E. C. Ashby and J. P. Carbotte, Phys. Rev. B **89**, 245121 (2014).

[9] E. Martino, I. Crassee, G. Eguchi, D. Santos-Cottin, R. D. Zhong, G. D. Gu, H. Berger, Z. Rukelj, M. Orlita, C. C. Homes, and A. Akrap, Phys. Rev. Lett. **122**, 217402 (2019).

[10] L. Moreschini, J. C. Johannsen, H. Berger, J. Denlinger, C. Jozwiak, E. Rotenberg, K. S. Kim, A. Bostwick, and M. Grioni, Phys. Rev. B **94**, 081101(R) (2016).

[11] T. Liang, J. Lin, Q. Gibson, S. Kushwaha, M. Liu, W. Wang, H. Xiong, J. A. Sobota, M. Hashimoto, P. S. Kirchmann, Z.-X. Shen, R. J. Cava, and N. P. Ong, Nat. Phys. **14**, 451 (2018).

[12] R. Y. Chen, S. J. Zhang, J. A. Schneeloch, C. Zhang, Q. Li, G. D. Gu, and N. L. Wang, Phys. Rev. B **92**, 075107 (2015).

[13] R. Y. Chen, Z. G. Chen, X. Y. Song, J. A. Schneeloch, G. D. Gu, F. Wang, and N. L. Wang, Phys. Rev. Lett. **115**, 176404 (2015).

[14] D. Santos-Cottin, M. Padlewski, E. Martino, S. B. David, F. Le Mardelé, F. Capitani, F. Borondics, M. D. Bachmann, C. Putzke, P. J. W. Moll, R. D. Zhong, G. D. Gu, H. Berger, M. Orlita, C. C. Homes, Z. Rukelj, and A. Akrap, Phys. Rev. B **101**, 125205 (2020).

[15] C. J. Tabert, J. P. Carbotte, and E. J. Nicol, Phys. Rev. B **93**, 085426 (2016).

[16] C. J. Tabert and J. P. Carbotte, Phys. Rev. B **93**, 085442 (2016).

[17] D. K. Mukherjee, D. Carpentier, and M. O. Goerbig, Phys. Rev. B **100**, 195412 (2019).

[18] H.-Z. Lu, S.-B. Zhang, and S.-Q. Shen, Phys. Rev. B **92**, 045203 (2015).

[19] R. Okugawa and S. Murakami, Phys. Rev. B **89**, 235315 (2014).

[20] D. J. Singh, *Planewaves, Pseudopotentials and the LAPW Method* (Kluwer Adademic, Boston, 1994).

[21] D. Singh, Phys. Rev. B **43**, 6388 (1991).

[22] P. Blaha, K. Schwarz, G. K. H. Madsen, D. Kvasnicka, and J. Luitz, *WIEN2k, An Augmented Plane Wave Plus Local Orbitals Program for Calculating Crystal Properties* (Techn. Universität Wien, Austria, 2001).

[23] H. Xiong, J. A. Sobota, S. L. Yang, H. Soifer, A. Gauthier, M. H. Lu, Y. Y. Lv, S. H. Yao, D. Lu, M. Hashimoto, P. S. Kirchmann, Y. F. Chen, and Z. X. Shen, Phys. Rev. B **95**, 195119 (2017).

[24] S. A. Miller, I. Witting, U. Aydemir, L. Peng, A. J. E. Rettie, P. Gorai, D. Y. Chung, M. G. Kanatzidis, M. Grayson, V. Stevanović, E. S. Toberer, and G. J. Snyder, Phys. Rev. Appl. **9**, 014025 (2018).

[25] Z. Fan, Q.-F. Liang, Y. B. Chen, S.-H. Yao, and J. Zhou, Sci. Rep. **7**, 45667 (2017).

[26] S. Tchoumakov, M. Civelli, and M. O. Goerbig, Phys. Rev. B **95**, 125306 (2017).

[27] T. M. McCormick, I. Kimchi, and N. Trivedi, Phys. Rev. B **95**, 075133 (2017).

[28] S.-Q. Shen, *Topological Insulators: Dirac Equation in Condensed Matter*, Springer Series in Solid-State Sciences Vol. 187 (Springer, Singapore, 2017).

[29] N. W. Ashcroft and N. Mermin, *Solid State Physics* (Saunders College, Philadelphia, PA, 1976).

[30] M. Dressel and G. Grüner, *Electrodynamics of Solids* (Cambridge University Press, New York, NY, 2002).

[31] G. D. Mahan, *Many-Particle Physics* (Plenum, New York, 1993).

[32] I. Kupčić, Z. Rukelj, and S. Barišić, J. Phys.: Condens. Matter **25**, 145602 (2013).

[33] I. Kupčić, G. Nikšić, Z. Rukelj, and D. Pelc, Phys. Rev. B **94**, 075434 (2016).

[34] T. Morinari, T. Himura, and T. Tohyama, J. Phys. Soc. Jpn. **78**, 023704 (2009).

[35] S. Rusponi, M. Papagno, P. Moras, S. Vlaic, M. Etzkorn, P. M. Sheverdyaeva, D. Pacilé, H. Brune, and C. Carbone, Phys. Rev. Lett. **105**, 246803 (2010).

[36] H. Ryu, S. Y. Park, L. Li, W. Ren, J. B. Neaton, C. Petrovic, C. Hwang, and S.-K. Mo, Sci. Rep. **8**, 15322 (2018).

[37] J. Park, G. Lee, F. Wolff-Fabris, Y. Y. Koh, M. J. Eom, Y. K. Kim, M. A. Farhan, Y. J. Jo, C. Kim, J. H. Shim, and J. S. Kim, Phys. Rev. Lett. **107**, 126402 (2011).

[38] Y.-X. Wang and F. Li, Phys. Rev. B **101**, 195201 (2020).